ACCSCIENCE PUBLISHING

International Journal of Bioprinting

RESEARCH ARTICLE

# Pyridinium-based acrylate additives for multifunctional 3D-printable photosensitive resins with antibacterial, antistatic, and high-strength properties

**Qiaoling Zhang[1†], Tongyi Wu[1†], Taojun Lin[1], Xiangqin Ding[1], Zhiwei Zhang[1], Jianqing Liang[1], Rong Li[1], Xiaomin Zhang[2*], Guoqiao Lai[1*], and Qiu Chen[1*]**

[1]College of Material, Chemistry, and Chemical Engineering, Hangzhou Normal University, Hangzhou, Zhejiang, China

[2]Zhejiang Xunshi Technology Co., Ltd., Shaoxing, Zhejiang, China

## Abstract

The increasing demand for biomaterial safety in precision medical device manufacturing and electronic packaging highlights the critical need for the rapid development of 3D-printable photosensitive resins that offer high mechanical strength, durable antibacterial effectiveness, and consistent antistatic properties. Traditional approaches involving multiple additives often result in poor compatibility, low success rates in 3D printing, compromised functionality or mechanical properties, and insufficient functional stability and longevity. To address this challenge, we introduce a new category of pyridinium-based acrylate photosensitive additives. By adjusting the quantity of pyridinium functional groups within a single additive, we have successfully achieved multifunctionalization of the 3D printing resin. The findings indicated that the pyridinium-based acrylate additive endows the 3D-printed photosensitive resin with exceptional antibacterial efficacy (>99.99% against *Escherichia coli* and *Staphylococcus aureus*), strong antistatic performance (resistance: $10^9$ Ω), and high tensile strength (40.86 MPa). Furthermore, the resin demonstrated enduring and consistent antibacterial and antistatic properties. The study suggests that the novel pyridinium-based acrylate photosensitive additive can achieve a breakthrough in enhancing multifunctional 3D printing resin performance.

***Keywords:*** Antibacterial; Antistatic; Photosensitive resin; Pyridine-based acrylic ester; UV-light curing 3D printing

†These authors contributed equally to this work

***Corresponding authors:**
Xiaomin Zhang (zhangxiaomin@sprintray.cn)

Guoqiao Lai (20020549@hznu.edu.cn)

Qiu Chen (20070057@hznu.edu.cn)

**Citation:** Zhang Q, Wu T, Lin T, *et al.* Pyridinium-based acrylate additives for multifunctional 3D-printable photosensitive resins with antibacterial, antistatic, and high-strength properties. *Int J Bioprint.* 2025;11(5):315-332. doi: 10.36922/IJB025280279

**Received:** July 10, 2025
**Revised:** August 14, 2025
**Accepted:** August 22, 2025
**Published online:** August 25, 2025



## 1. Introduction

Photocuring 3D printing technology has gained widespread application across multiple fields in recent years due to its low energy consumption and high fabrication precision.[1-3] However, the mechanical properties of printed parts, including strength, toughness, and modulus, are often inadequate due to limitations in existing photosensitive resins, restricting their use in demanding production applications.[4-6] Therefore, it is essential

to modify photosensitive resins with functional additives to improve their mechanical performance.[7] Additionally, the polymer surfaces of these printed parts are prone to microbial colonization during storage, transportation, and use, posing biological safety risks. Moreover, the insulating properties of polymeric materials can result in electrostatic accumulation, compromising the dimensional stability and functionality of precision medical and electronic devices.[8–10] To address these challenges, the development of multifunctional modifiers for photosensitive resin systems that can enhance mechanical properties, prevent microbial growth, and reduce static buildup has become a crucial research focus to meet the market demand for high-performance, multifunctional 3D printing materials.

Recently, various pyridinium salts have emerged as multifunctional modifiers with combined antibacterial and antistatic properties.[11] Their antibacterial mechanism primarily relies on a cationic contact-killing effect: the quaternary ammonium cation ($[R_4N]^+$), where R is the substituent in the pyridinium structure, electrostatically binds to negatively charged microbial cell membranes, membrane protein hydrolysates, and other anionic molecules. Simultaneously, their hydrophobic chains penetrate the hydrophobic core of the bacterial membrane, disrupting its structure and denaturing critical proteins (e.g., structural proteins and enzymes), ultimately leading to microbial death.[12,13] Concerning antistatic performance, the quaternary ammonium groups of pyridinium salts interact with negatively charged environmental particles (e.g., dust and ions) to achieve charge neutralization. Additionally, their hygroscopicity promotes the adsorption of water molecules onto the material surface, forming ionic conductive pathways that effectively dissipate static charges.[14,15] However, the current pyridinium-based antibacterial/antistatic agents still encounter practical challenges, including limited chemical reactivity, insufficient thermal stability, and short functional longevity.

The integration of pyridinium salt additives into photopolymerization-based 3D printing systems poses challenges. The limited absorption range of pyridinium salts (<360 nm) impedes their direct initiation of visible-light polymerization. Despite the potential redshift in absorption (375–560 nm) through charge-transfer complex formation with electron donors, this approach adds complexity to the system, leading to compatibility issues, phase separation risks, and necessitates precise polymerization kinetics control.[16,17] Moreover, excessive or inappropriate addition can negatively impact the mechanical properties (e.g., strength and toughness) of the cured material.[18] Therefore, optimizing the molecular structure, loading amount, and compatibility with the resin matrix is crucial to develop pyridinium-modified photosensitive resins with enhanced antibacterial and antistatic properties, as well as targeted mechanical performance. This optimization is essential to strike a balance between multifunctionality, processability, and overall performance of the final printed components.

Building upon this groundwork, we developed a new pyridinium-based acrylate photosensitive additive by incorporating pyridine into the acrylate backbone, followed by quaternization. Through tailored chemical modification of the pyridinium functional groups, we synthesized two acrylate reactive monomers using isophorone diisocyanate (IPDI; a monopyridinium salt functional monomer [IPDI'-PS] and a bis-pyridinium salt functional monomer [IPDI"-PS]) as the primary reactant. These monomers were then blended with reactive diluents, oligomers, and a photoinitiator to create photosensitive resins, which were subsequently photopolymerized using digital light processing (DLP) 3D printing. We systematically assessed the mechanical properties of the printed components and explored the impact of varying the concentration of the pyridinium-based acrylate additives (IPDI'-PS and IPDI"-PS) on the antibacterial and antistatic properties of the prints. Finally, we conducted a comparative evaluation of the overall performance between the 3D-printed photosensitive resins containing IPDI'-PS and those containing IPDI"-PS.

## 2. Materials and methods

### 2.1. Materials

Isophorone diisocyanate (IPDI), dibutyl tin dilaurate (DBTDL), 1,3-propanediol (PDO), trimethylolpropane (TMP), 4-aminopyridine (4-AP), iodomethane ($CH_3I$), 4-acryloyl morpholine (ACMO), cyclotrimethylolpropane acrylate (CTFA), acetonitrile (MeCN), and hydroquinone were procured from Sinopharm Chemical Reagent Co., Ltd. (China). Methyl methacrylate-2-hydroxyethyl ester (HEMA), diphenyl (2,4,6-trimethylbenzoyl) oxime (TPO), and N,N-dimethylformamide (DMF) were obtained from Beijing Warwick Chemical Co., Ltd. (China). *Staphylococcus aureus* and *Escherichia coli* were acquired from Shanghai Macklin Biochemical Co., Ltd. (China).

### 2.2. Synthesis of the pyridinium-based acrylate photosensitive additive

Monofunctional (IPDI'-PS) and bifunctional (IPDI"-PS) pyridinium salt acrylate reactive monomers were synthesized by reacting IPDI with different alcohols (PDO and TMP), followed by introducing photosensitive unsaturated double bonds via HEMA, and finally end-capping with 4-AP and quaternization. The specific procedure is as follows.

#### 2.2.1. Synthesis of monofunctional pyridinium-based acrylate photosensitive additive (IPDI'-PS)

As displayed in Line 1 of Figure 1, a three-necked flask containing 0.1 mol of PDO, 0.1 g of DBTDL, 0.1 g of hydroquinone, and 50 mL of DMF was placed in an ice–water bath. Subsequently, 0.2 mol of IPDI was added dropwise. After complete addition, the mixture was heated to 35°C and reacted for 3 h, resulting in the formation of the precursor OCN-PDO-NCO. Following this, 0.1 mol of HEMA was added dropwise and allowed to react for 2 h to introduce a photosensitive group successfully. Then, 0.2 mol of 4-AP was added to cap the remaining isocyanate groups (–NCO) in the system. The reaction progress was monitored using Fourier-transform infrared (FTIR) spectroscopy or chemical titration until no detectable –NCO groups were present, indicating complete end-capping and the formation of the intermediate HEMA-PDO-AP. Finally, $CH_3I$ was added for the quaternization of the intermediate. Upon completion of the reaction, the solvent and volatile byproducts were removed under reduced pressure. The crude product was dried under vacuum at 60°C for 12 h, resulting in the production of the IPDI'-PS additive.

#### 2.2.2 Synthesis of the IPDI'-PS additive

As displayed in Line 2 of Figure 1, a three-necked flask was charged with 0.1 mol of TMP, 0.2 g of DBTDL, 0.2 g of hydroquinone, and 50 mL of DMF and placed in an ice–water bath. Subsequently, 0.3 mol of IPDI was added dropwise. The reaction was conducted at 60°C for 3 h, resulting in the formation of the precursor TMP-TriNCO. Subsequently, 0.1 mol of HEMA was added dropwise and allowed to react for 2 h to introduce a photosensitive group. Following this, 0.3 mol of 4-AP was added to end-cap the remaining isocyanate groups (–NCO). The reaction progress was monitored using FTIR spectroscopy or chemical titration until no –NCO groups were detectable, indicating complete end-capping and the formation of the intermediate HEMA-TMP-DiAP. Finally, $CH_3I$ was then added for quaternization of the intermediate. Upon completion of the reaction, the solvent and volatile byproducts were removed under reduced pressure. The crude product was dried under vacuum at 60°C for 12 h, yielding the bis-pyridinium salt functional acrylate reactive monomer (IPDI"-PS).

### 2.3. Preparation of 3D-printable photosensitive resins

According to the feed ratios specified in Tables 1 and 2, the oligomer (tris(2-hydroxyethyl) isocyanurate triacrylate), the reactive diluents CTFA and ACMO, the pyridinium-based acrylate photosensitive additive (either IPDI'-PS or IPDI"-PS), and the photoinitiator TPO were added sequentially to an opaque container. The formulated 3D-printable photosensitive resin was then mixed uniformly using a mechanical stirrer, followed by sonication to remove air bubbles. Finally, the resin was sealed and stored in light-protected conditions.

### 2.4. Photopolymerization of 3D-printable photosensitive resins

The 3D printable photosensitive resins were poured into the resin vat of a DLP 3D printer (AccuFab-D1; Hangzhou Shining 3D Tech Co., Ltd., China) for printing. Subsequently, the printed samples were washed with anhydrous ethanol to eliminate surface-uncured resin and subsequently cured in a UV chamber for 5 min (Figure 2a and b).

### 2.5. Characterization and testing

#### 2.5.1. $^1$H nuclear magnetic resonance characterization

$^1$H nuclear magnetic resonance (NMR) spectra of the synthesized pyridinium-based acrylate photosensitive additive were recorded on an AVANCE AV 400 MHz spectrometer (Bruker, Germany) using $CDCl_3$ or DMSO-$d_6$ as the solvent.

#### 2.5.2. Fourier-transform infrared characterization

Fourier-transform infrared (FTIR) spectra of the pyridinium-based acrylate photosensitive additive, the 3D-printable photosensitive resins, and the printed samples were recorded on a Nicolet 5700 spectrometer (Nicolet, United States of America [USA]) in the range of 4000–500 $cm^{-1}$.

#### 2.5.3. Curing shrinkage testing

The curing shrinkage of the 3D-printable photosensitive resins was measured according to ISO 3521:1997 using an HTY-300SL multifunctional solid–liquid densitometer (Dedu, China). Measurements were performed according to the sample state as follows:

(i) Solid samples: The measurement chamber was filled with deionized water and equilibrated on the balance. The wire basket was immersed. After the bubble disappearance, the balance was tared ("0"). The solid sample was placed on the basket cover. Following the "OK" display, "MEMORY" was pressed. The sample was then fully immersed in water within the basket. After achieving a bubble-free state and "OK" display, "MEMORY" was pressed to record the measurement.

(ii) Liquid samples: The base plate, stand, and hook were positioned on the balance and tared ("0"). The sinker was suspended from the stand's center. After the "OK" display, "MEMORY" was pressed. A beaker containing the liquid photopolymer resin was

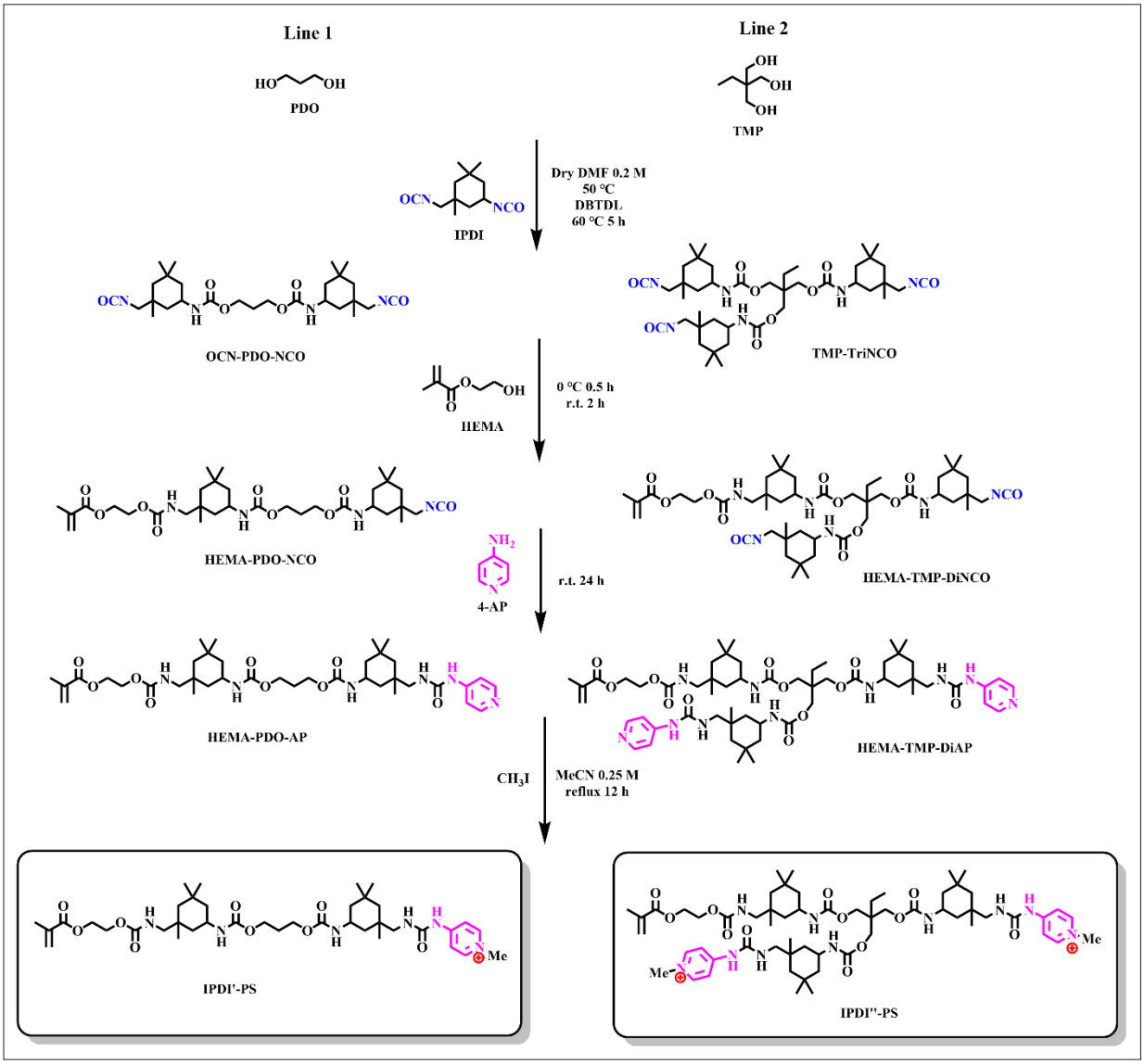


**Figure 1.** Synthesis of the pyridinium-based acrylate photosensitive additives: IPDI'-PS and IPDI"-PS. Abbreviations: 4-AP, 4-aminopyridine; $CH_3I$, Iodomethane; DBTDL, dibutyl tin dilaurate; DMF, N,N-dimethylformamide; HEMA, methyl methacrylate-2-hydroxyethyl ester; IPDI'-PS, monopyridine salt functional group photosensitive additive monomer; IPDI"-PS, bipyridine salt functional group photosensitive additive monomer; MeCN, acetonitrile; PDO, 1,3-propanediol; TMP, trimethylolpropane.

**Table 1. Formulation of 3D-printable photosensitive resins using IPDI'-PS**

| Resin | Polyurethane acrylate (wt%) | CTFA (wt%) | ACMO (wt%) | IPDI'-PS (wt%) | TPO (wt%) |
|---|---|---|---|---|---|
| PR- IPDI'-PS-1 | 50 | 35 | 24.5 | 0 | 0.5 |
| PR- IPDI'-PS-2 | 50 | 35 | 22.5 | 2 | 0.5 |
| PR- IPDI'-PS-3 | 50 | 35 | 20.5 | 4 | 0.5 |
| PR- IPDI'-PS-4 | 50 | 35 | 18.5 | 6 | 0.5 |
| PR- IPDI'-PS-5 | 50 | 35 | 16.5 | 8 | 0.5 |
| PR- IPDI'-PS-6 | 50 | 35 | 14.5 | 10 | 0.5 |

Abbreviations: ACMO, 4-acryloyl morpholine; CTFA, cyclotrimethylolpropane acrylate; IPDI'-PS, monopyridine salt functional group photosensitive additive monomer; PR-IPDI'-PS-1, blank control (3D printed photosensitive resin without pyridine salt photosensitive additive); PR-IPDI'-PS-2 to 6, 3D printed photosensitive resins with different contents of monofunctional pyridine salt photosensitive additives; TPO, diphenyl (2,4,6-trimethylbenzoyl) oxime.

positioned beneath the sinker, which was tilted and fully immersed. Following the bubble disappearance at the liquid surface, "MEMORY" was pressed to record the measurement.

Each measurement was repeated three times, and the average value was used to calculate the curing shrinkage according to **Equation (I)**:

$$V_s = \frac{\rho_c - \rho_l}{\rho_c} \times 100\% \quad \text{(I)}$$

where $V_s$ is the curing shrinkage, $\rho_l$ is the density of the liquid photopolymer resin, and $\rho_c$ is the density of the cured 3D-printed material.

#### 2.5.4. Gel content testing

The gel content of the elastomer was measured by solvent extraction before and after thermal curing. Samples, with dimensions of 10 × 10 × 0.65 mm$^3$, were immersed in toluene at 25°C for 48 h, followed by drying in an oven at 80°C for 24 h. The weights of the original samples ($m_0$), the swollen samples ($m_s$), and the dried samples ($m_d$) were recorded. Additionally, the crosslink density ($\nu_e$) and the average molecular weight of the polymer between the crosslinks ($M_c$) were calculated by using the Flory–Rehner equation (**Equations II–IV**):

$$\nu_e = \frac{-\left[\ln\left(1 - V_r\right) + V_r + \chi V_r^2\right]}{V_0\left(V_r^{\frac{1}{3}}\right)} \quad \text{(II)}$$

where

$$V_r = \frac{\frac{m_d}{\rho_2}}{\frac{m_d}{\rho_2} + \frac{m_s - m_d}{\rho_1}} \quad \text{(III)}$$

$$M_c = \frac{\rho_2}{\nu_e} \quad \text{(IV)}$$

where $V_r$ denotes the volume fraction of the samples, $\chi$ denotes the Flory–Huggins polymer–solvent interaction parameter, and $V_0$ denotes the molar volume of toluene (106.2 cm$^3$/mol). The values obtained from this equation were used in the derivation, where $\rho_1$ (0.865 g/mol) represents the density of the solvent and $\rho_2$ (1.113 g/mol) represents the density of the polymer.

#### 2.5.5. Hardness testing

Hardness of the 3D-printed specimens was measured according to ISO 868:2003 using an LX-D Shore D durometer (Shanghai Luling Instrument Factory, China). Individual samples (10 × 10 × 5 mm$^3$) were placed on a rigid, stable horizontal surface. The durometer's presser foot was applied to the sample surface to obtain hardness readings. Five measurements were performed per sample group, and the average value was reported.

#### 2.5.6. Tensile testing

Tensile strength and elongation at break of the 3D-printed specimens were measured according to ISO 527-1:2019 using an AI-7000-MU1 universal testing machine (Gotech Testing Machines Co., Ltd., China) equipped with a 5000 N load cell. Specimens were machined into a dumbbell shape with a gauge section measuring 20 × 4 × 3 mm$^3$. Five specimens per group were tested, and the average values were reported.

#### 2.5.7. Heat distortion temperature testing

The heat deflection temperature (HDT) of the 3D-printed specimens was measured according to ISO 75 using a GT-HV2000-C3W heat deflection tester (Gotech Testing Machines Co., Ltd., China). Rectangular specimens (100 × 10 × 4 mm$^3$) were tested in an oil bath with a heating rate of 120°C/h, a deflection limit of 0.34 mm, and an applied

**Table 2. Formulation of 3D-printable photosensitive resins using IPDI"-PS**

| Resin | Polyurethane acrylate (wt%) | CTFA (wt%) | ACMO (wt%) | IPDI"-PS (wt%) | TPO (wt%) |
|---|---|---|---|---|---|
| PR- IPDI"-PS-1 | 50 | 35 | 24.5 | 0 | 0.5 |
| PR- IPDI"-PS-2 | 50 | 35 | 22.5 | 2 | 0.5 |
| PR- IPDI"-PS-3 | 50 | 35 | 20.5 | 4 | 0.5 |
| PR- IPDI"-PS-4 | 50 | 35 | 18.5 | 6 | 0.5 |
| PR- IPDI"-PS-5 | 50 | 35 | 16.5 | 8 | 0.5 |
| PR- IPDI"-PS-6 | 50 | 35 | 14.5 | 10 | 0.5 |

Abbreviations: ACMO, 4-acryloyl morpholine; CTFA, cyclotrimethylolpropane acrylate; IPDI"-PS, bipyridine salt functional group photosensitive additive monomer; PR-IPDI"-PS-1, blank control (3D printed photosensitive resin without pyridine salt photosensitive additive); PR-IPDI"-PS-2 to 6, 3D printed photosensitive resins with different contents of bipyridine salt photosensitive additives; TPO, diphenyl (2,4,6-trimethylbenzoyl) oxime.

stress of 0.455 MPa (66 psi). Three specimens were tested per group, and the average value was reported.

#### 2.5.8. Thermogravimetric analysis

Thermal stability of the 3D-printed specimens was determined using a Q500 thermogravimetric analyzer (TA Instruments, USA). Samples (~5 mg) were loaded into alumina crucibles and heated under a nitrogen atmosphere from 25 to 600°C at a rate of 20°C/min. Thermogravimetric (TG) curves were recorded.

#### 2.5.9. Penetration depth testing

The resin to be tested was placed in a small tank, and the laser power was set to 300 mW. The scanning distance was set to 0.08 mm, and the resin running temperature was set to 25 °C. A series of different scanning times was then set, and a single-layer 20 × 20 $mm^2$ square sheet was made using the plane scanning method. The thickness of the sheet was measured with a thickness gauge. Subsequently, the square sheet was subjected to a cleaning process involving a mixture of ethanol and isopropanol. Thereafter, the sample was UV-cured, as previously described. Following these steps, the thickness of the sheet was measured once more, and the penetration depth ($D_p$) was derived in accordance with the Lambert–Beer law using **Equation (V)**:

$$C_d = D_p \times \ln \frac{E}{E_c} \quad \text{(V)}$$

where $C_d$ denotes the depth of cure, $E$ represents the exposure energy, and $E_c$ signifies the critical exposure energy.[19]

#### 2.5.10. Antistatic property testing

Surface resistivity of the 3D-printed specimens was measured in accordance with ISO 3915 using a CXT5015 surface resistivity meter (Xinyang Electronics Co., Ltd., China). This measurement serves as an indicator of antistatic performance, as electrostatic charge generation, accumulation, and dissipation are directly governed by a material's electrical conductivity. Resistivity values were recorded at 1, 14, and 30 days after specimen preparation. Five measurements were performed per time interval, and the average value was calculated.

#### 2.5.11. Antibacterial property testing

Antibacterial activity of the samples was evaluated against *E. coli* and *S. aureus* according to ISO 22196:2007 using the colony counting method.

The test sample was put into a petri dish, and 30 μL of bacterial liquid was added dropwise to the front side of the test sample membrane. A non-toxic and non-resistant polyethylene (PE) film (50 × 50 $mm^2$) was used to cover the top of the bacterial liquid, and the film was gently pressed to push the bacterial liquid to be in close contact with the sample to ensure that the bacteria were tightly affixed to the surface of the sample. The sample was finally cultivated in a $CO_2$ thermostatic incubator at 37°C. The test sample was then incubated for 8 h with an LB liquid medium to elute the eluted bacterial liquid. After 8 h of incubation, bacteria on the sample's surface were eluted with LB liquid medium, and the eluted bacterial liquid was collected. The test sample specification was a rectangle of 80 × 80 × 5 $mm^3$. After incubation, the culture broth and eluate were diluted with sterile water to the appropriate concentration. Then, 30 μL of the broth was pipetted into the LB solid medium, spread evenly with a spreader, and sealed with a sealing film. The solid medium was placed upside down in a $CO_2$ incubator at 37°C for 24 h, and the number of colonies on the solid medium was counted to calculate the antibacterial rate. The antibacterial rate was calculated using **Equation (VI)**:

$$G = \frac{A - B}{A} \times 100\% \quad \text{(VI)}$$

where $G$ is the antibacterial rate of the sample, $A$ is the colony count of the control group, and $B$ is the colony count of the experimental sample group.

#### 2.5.12. Statistical analysis

All quantitative data are expressed as the mean ± standard deviation from at least three independent experiments ($n \geq 3$). Graphs were generated using OriginPro 2022 software (OriginLab, USA), with error bars representing standard deviation. Statistical significance between groups was determined by one-way analysis of variance (ANOVA) followed by Tukey's post hoc test, with $p < 0.05$ considered statistically significant.

## 3. Results and discussion

### 3.1. Synthesis of the photosensitive additives IPDI'-PS and IPDI"-PS

Comparison of the FTIR spectra with those of the raw material IPDI (Figure 2c) revealed identical spectral changes for both the mono-pyridinium salt (IPDI'-PS) and bis-pyridinium salt (IPDI"-PS) systems. The complete disappearance of the characteristic isocyanate (–NCO) peak at 2246 $cm^{-1}$ indicates the full consumption of –NCO groups in IPDI and successful end-capping. Key characteristic peaks corresponding to the formation of urethane bonds via the –NCO/–OH reaction appeared: the C=O stretching vibration at ~1680 $cm^{-1}$, the strong N–H stretching vibration absorption at ~3313 $cm^{-1}$, and the characteristic peaks for N–H bending vibration coupled

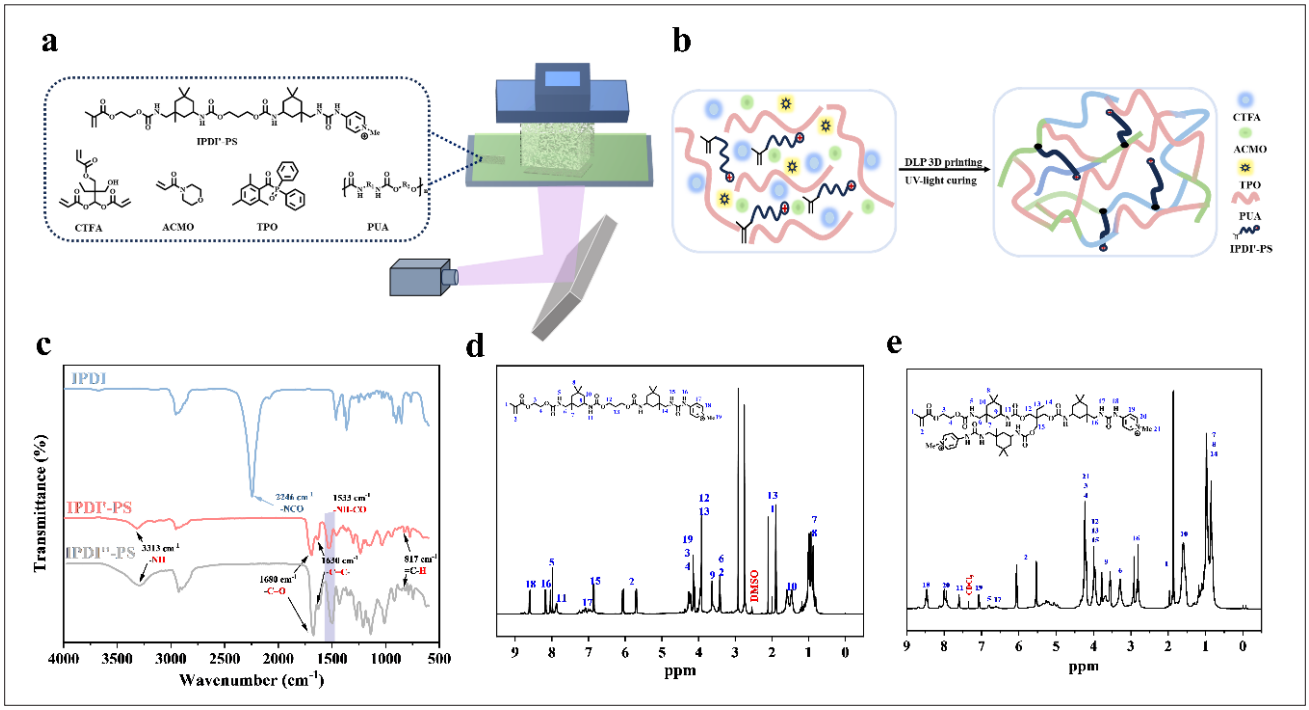


**Figure 2.** DLP 3D printing and additives characterization. (a) Schematic of DLP 3D printing. (b) UV-curing mechanism of the IPDI'-PS system. (c) FTIR spectra of the pyridinium-based acrylate photosensitive additives IPDI'-PS and IPDI"-PS. (d) $^1$H NMR spectrum of IPDI'-PS in DMSO-$d_6$. (e) $^1$H NMR spectrum of IPDI"-PS in $CDCl_3$. Abbreviations: ACMO, 4-acryloyl morpholine; CTFA, cyclotrimethylolpropane acrylate; DLP, digital light processing; IPDI, isophorone diisocyanate; IPDI'-PS, monopyridine salt functional group photosensitive additive monomer; TPO, diphenyl (2,4,6-trimethylbenzoyl) oxime; PUA, polyurethane acrylate; UV-light, ultraviolet light; $^1$H NMR, $^1$H nuclear magnetic resonance.

with C–N stretching vibration at ~1533 cm$^{-1}$. Furthermore, the emergence of the =C–H bending vibration peak of the alkene group at ~817 cm$^{-1}$ confirms the successful grafting of the photosensitive group. The appearance of these characteristic peaks and their associated functional groups aligned with the expected structures of the target products, IPDI'-PS and IPDI"-PS. The successful synthesis was further confirmed by $^1$H NMR analysis (Figure 2d and e).

### 3.2. Double bond conversion, volumetric shrinkage, and penetration depth

The characteristics of the photosensitive resin itself, such as its curability, cure shrinkage, and printing accuracy, play a crucial role in influencing the material performance in DLP 3D printing. Initially, the FTIR spectra (Figure 3a) of the uncured liquid resins were compared with those of samples post-photopolymerization and UV post-curing. The distinctive C=C double bond absorption peak at 1643 cm$^{-1}$ was significantly reduced after photopolymerization, indicating a substantial C=C conversion (>99%) and efficient photocuring. These findings validate that the formulation utilized in this study improved the reactivity and integration of photosensitive components within the curing system, leading to enhanced photoconversion.[20,21] High conversion rates are essential for establishing a dense crosslinked network and achieving optimal material performance.[22]

During photopolymerization-based 3D printing, photosensitive resins transform from liquid monomers to a solid crosslinked network. This process inherently causes significant volume shrinkage due to reduced intermolecular distances.[23] Consequently, cure shrinkage plays a crucial role in determining printing accuracy, dimensional stability, and final part performance. Excessive shrinkage can result in internal stress buildup, warping, and interlayer delamination, significantly affecting the fabrication of high-precision devices.[24] Volumetric shrinkage primarily stems from the shortening of molecular distances during covalent bond formation in C=C double bond polymerization, with its extent determined by the total concentration of C=C bonds and the final conversion within the system.[25–27]

To systematically evaluate the impact of the pyridinium molecular structure on curing shrinkage, we compared the modification effects of IPDI'-PS containing a single pyridinium group and IPDI'-PS containing dual pyridinium groups across the same loading range. Figure 3b illustrates that the addition of photosensitizing

additives with varying pyridinium group numbers effectively reduced cure shrinkage compared to the unmodified resin (control group, 10.81% shrinkage). The reduction in shrinkage was dependent on the molecular structure, displaying a consistent decrease as the additive loading increased. At a 10 wt% loading, shrinkage minimized to 7.20%, marking a significant 33.4% reduction compared with the control. This decrease can be attributed to three main factors. Firstly, as a non-polymerizing component, IPDI'-PS diluted the concentration of polymerizable C=C bonds per unit volume, thereby reducing the total amount of shrinkage-contributing monomers/oligomers. Secondly, FTIR results confirmed a high C=C conversion (>99%), ensuring that the dilution effect translated effectively into reduced shrinkage and improved dimensional accuracy of printed parts. In contrast, the IPDI"-PS photosensitizing additive exhibited a more pronounced effect in suppressing cure shrinkage, which decreased continuously at higher loadings. Notably, even at a low 2 wt% loading, IPDI"-PS exhibited a clear modification effect, reducing shrinkage to 9.61% (an 11.1% reduction). With a 10 wt% loading, shrinkage further decreased to 6.05%, achieving a substantial 44.0% reduction compared to that of the control. The superior efficiency of IPDI"-PS arises from its role as a nonshrinking component that dilutes the C=C bond concentration. Additionally, its dipyridinium salt structure provides higher functionality, potentially altering the $\nu_e$ or network architecture upon network participation or influence, thereby further suppressing shrinkage behavior.

Furthermore, the Dp of the photosensitive resins was assessed using a DLP 3D printer to evaluate their suitability for creating intricate structures with high precision and their potential as DLP 3D printing materials.[28] As the curing degree increased, the single-layer cure thickness of the resin also increased. Figure 3c illustrates that the unmodified resin (control) had a Dp value of 0.1776. In contrast, the Dp values of resins modified with either IPDI'-PS or IPDI"-PS progressively decreased with increasing additive loading, consistently falling within an intermediate range between high and low Dp. This suggests that the resins incorporating pyridinium-based acrylate photosensitizing additives can maintain relatively fast printing speeds while enabling the fabrication of complex structures with enhanced resolution.

Collectively, these results demonstrate that the intrinsic properties of the photosensitive resins prepared in this study are compatible with the requirements of DLP 3D printing.

### 3.3. Thermal properties

To systematically evaluate the impact of the pyridinium group count (IPDI'-PS vs. IPDI"-PS) on the thermal stability of 3D-printed materials, HDT measurements and thermogravimetric analysis (TGA) were conducted. The HDT demonstrated a notable correlation with the loading of pyridinium additives (IPDI'-PS and IPDI"-PS) (Figure 3d).

For the IPDI'-PS system, the HDT increased with additive loading up to 6 wt%, peaking at 43.5°C. This improvement of 1.5°C over the unmodified reference system highlights the positive impact of optimal IPDI'-PS loading on thermal deformation resistance. Beyond 6 wt%, the HDT decreased, which is attributed to the effective participation of IPDI'-PS in the reaction and the optimization of the crosslinked network at optimal loadings. However, excessive loading may lead to pyridinium stacking and poor dispersion, compromising network homogeneity and introducing defects that reduce thermal stability.[29,30] In contrast, the IPDI"-PS system achieved its maximum HDT of 44.6°C (a 2.6°C increase over the control) at a lower loading of only 4 wt%, showcasing superior network densification efficiency at lower concentrations. However, the HDT progressively decreased beyond 4 wt% (41.9°C at 8 wt%; 40.9°C at 10 wt%), indicating that its more flexible molecular structure induces a milder disruption to network integrity. Although IPDI"-PS attained a higher peak HDT (44.6°C vs. 43.5°C) and required a lower optimal loading (4 wt% vs. 6 wt%) compared to IPDI'-PS, it exhibited a greater reduction at excessive loadings (–3.7°C at 10 wt% vs. –2.3°C for IPDI'-PS). This divergence in structure–property relationships stems from variances in pyridinium content and molecular rigidity.[31]

Thermogravimetric analysis (TGA) provided further insights into the thermal decomposition behavior of the materials (Figure 3e and f), specifically focusing on the initial decomposition temperature, defined as the temperature at 5% weight loss ($T_D5$). For the IPDI'-PS system, $T_D5$ initially increased and then decreased with higher IPDI'-PS loading. At 2 wt% loading, $T_D5$ was 158°C, peaking at 168°C at 6 wt% loading and decreasing to 153°C at 10 wt% loading. This suggests that IPDI'-PS effectively improved the thermal decomposition stability within the 6 wt% loading range, consistent with the HDT results. The IPDI"-PS system exhibited a unique trend: $T_D5$ presented an anomalous increase to 131.8°C at 4 wt% loading. However, at 2, 6, 8, and 10 wt% loadings, the $T_D5$ values were 113, 116, 115, and 107°C, respectively. These values were significantly lower than the peak observed at 4 wt% and notably below the corresponding $T_D5$ values of the IPDI'-PS system at equivalent loadings. This indicates that while IPDI"-PS notably raised the decomposition temperature at 4 wt%, its effectiveness in improving $T_D5$ was limited at other loadings (2, 6, 8, and 10 wt%). Furthermore, even

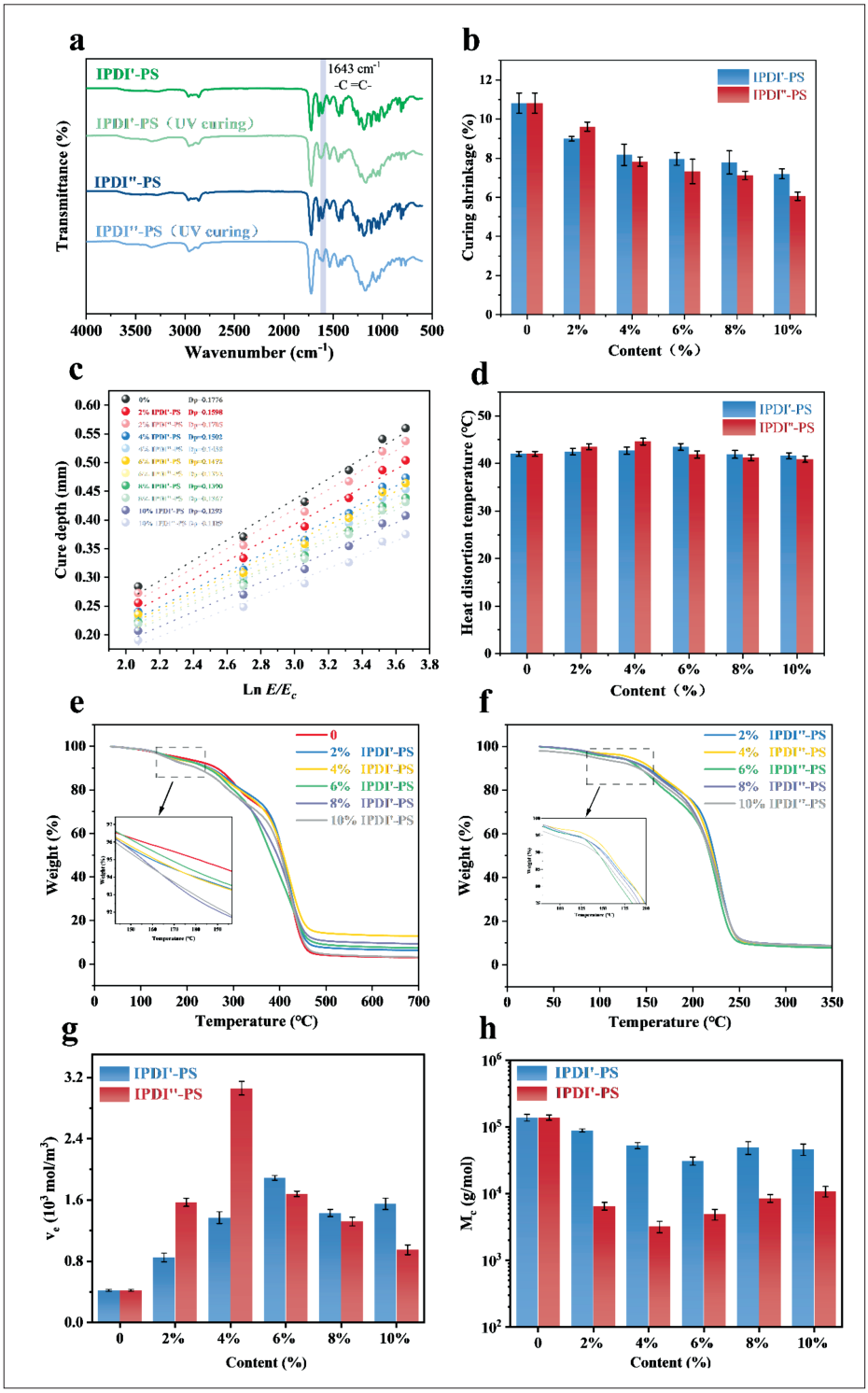


**Figure 3.** The effect of photosensitive additives on resin properties. (a) FTIR spectra of uncured liquid resins with IPDI'-PS or IPDI"-PS compared to their photocured counterparts. (b) Cure shrinkage of photosensitive resins at different loadings of IPDI'-PS or IPDI"-PS ($n$ = 5). (c) Dp of photosensitive resins at different loadings of IPDI'-PS or IPDI"-PS. (d) HDT of photosensitive resins modified with varying loadings of IPDI'-PS or IPDI"-PS ($n$ = 5). (e) TGA curves of photosensitive resins containing different loadings of IPDI'-PS. (f) TGA curves of IPDI"-PS-modified photosensitive resins at varying additive loadings. (g) Crosslink density ($v_e$) of photopolymers with varying loadings of IPDI'-PS or IPDI"-PS ($n$ = 5). (h) Average molecular weight between crosslinks ($M_c$) of photopolymers with varying loadings of IPDI'-PS or IPDI"-PS ($n$ = 5). Abbreviations: IPDI'-PS, 3D printed photosensitive resins of monopyridine salt photosensitive additive; IPDI"-PS, 3D printed photosensitive resins of bipyridine salt photosensitive additive.

the peak $T_D5$ achieved by IPDI"-PS (131.8°C) was notably lower than that of IPDI'-PS at its optimal loading (168°C). Overall, the TGA data suggested that IPDI'-PS generally performed less effectively than IPDI'-PS in enhancing the long-term thermal stability (resistance to decomposition) of the materials. However, the simultaneous peaks in both HDT and $T_D5$ for the IPDI"-PS system at 4 wt% confirmed a relatively optimal modification effect at this specific concentration.

Additionally, the $v_e$ and average molecular weight between crosslinks ($M_c$) of photopolymer resins containing different pyridinium salt additives were determined through swelling tests using the Flory–Rehner equation.[32] For the IPDI'-PS system, $v_e$ initially increased then decreased with increasing additive loading, peaking at 6 wt% (Figure 3g). This trend closely corresponds to the HDT and TGA ($T_D5$) results, where the maximum $v_e$ coincided with the highest HDT (43.5°C) and $T_D5$ (168°C). This suggests an optimal crosslink network density at 6 wt%, which effectively restricts polymer chain mobility, enhancing resistance to thermal deformation and decomposition. Excessive loading (> 6 wt%) likely leads to molecular crowding, compromising network homogeneity, and introducing stress concentration points, thereby reducing $v_e$ and diminishing thermal stability (as indicated by decreased HDT and $T_D5$). The $M_c$ data further support this mechanism (Figure 3h); at 6 wt%, $M_c$ reached its minimum (30,930 g/mol), indicating the shortest chain length between crosslinks and a rigid network structure essential for high thermal stability. Beyond 6 wt%, the significantly increased $M_c$ suggests enlarged crosslink spacing and network degradation, weakening thermal resistance. For IPDI"-PS, the peak $v_e$ ($3.06 \times 10^3$ mol/m³) was observed at a lower loading (4 wt%) due to the higher crosslinking efficiency per molecule conferred by its rigid pyridinium rings, facilitating rapid network densification ($v_e$ exceeded IPDI'-PS at equivalent concentrations). Beyond 4 wt%, excessively rigid groups induced molecular crowding and phase separation, expanding crosslink spacing and reducing $v_e$. Similarly, $M_c$ reached its minimum (3215 g/mol) at 4 wt%, confirming ultra-dense network formation. Above this threshold, progressively increasing $M_c$ indicated incremental network disruption from additive aggregation, resulting in a higher peak HDT (44.6 °C) but limited $T_D5$ improvement.

### 3.4. Mechanical properties

The mechanical properties of materials significantly impact wear resistance, compressive strength, and long-term dimensional stability, crucial for precision instruments and dental prosthetics. To assess the influence of two photosensitizing additives, IPDI'-PS and IPDI"-PS, on the mechanical properties of 3D-printed photosensitive resins, durometer measurements were conducted to determine sample hardness. Both systems exhibited similar trends (Figure 4a) as follows: hardness increased with higher pyridinium content but displayed saturation behavior beyond specific loadings. The increase was notably slower for IPDI'-PS beyond 8 wt%, while IPDI"-PS reached a plateau after 6 wt%. This observation suggests that pyridinium groups enhance network rigidity through ionic crosslinking, but excessive loading leads to an uneven distribution of crosslinking points due to steric hindrance, resulting in network defects.[33,34] Consequently, optimizing hardness is limited by the material's physical upper limit of $v_e$, necessitating a balance between molecular rigidity design and network integrity.

Regarding tensile strength, the material exhibited continuous improvement with increasing IPDI'-PS loading. At 10 wt% loading, the tensile strength increased significantly from 30.04 MPa (unmodified control) to 40.86 MPa, representing a 36.02% enhancement (Figure 4b and c). In contrast, the impact of IPDI"-PS loading on tensile strength exhibited an initial rise followed by a decline. A peak tensile strength of 37.96 MPa (26.32% increase over the control) was attained at 6 wt% loading. Beyond this concentration, the strength gradually decreased (Figure 4d and e). Notably, at higher IPDI"-PS loadings (8 and 10 wt%), a significant decrease in solubility within the system was observed, requiring notably extended mechanical stirring and sonication times. This solubility limitation is considered a key factor contributing to the decrease in tensile strength. Overall, IPDI'-PS demonstrated superior and more consistent performance in enhancing the tensile strength of the material (Figure 4f).

Both additives caused a significant decrease in the elongation at break (Figure 4c and e) at low loadings (2 wt%). This decrease is primarily due to the disruption of the native crosslinked structure of the resin by the additive molecules, which restricts molecular chain mobility.[35] However, as the loading increases, their effects diverge noticeably. Specifically, the continuous introduction of IPDI'-PS incorporates flexible chain segments into the system, enhancing molecular chain mobility and leading to a gradual recovery in the elongation at break. In contrast, increasing the IPDI"-PS loading only results in a brief initial increase, followed by a continuous decrease in the elongation at break, demonstrating its inferior effectiveness compared to that of IPDI'-PS in improving material toughness.

### 3.5. Antibacterial properties

Given the inherent antibacterial properties of pyridinium groups, this study systematically evaluated the antibacterial

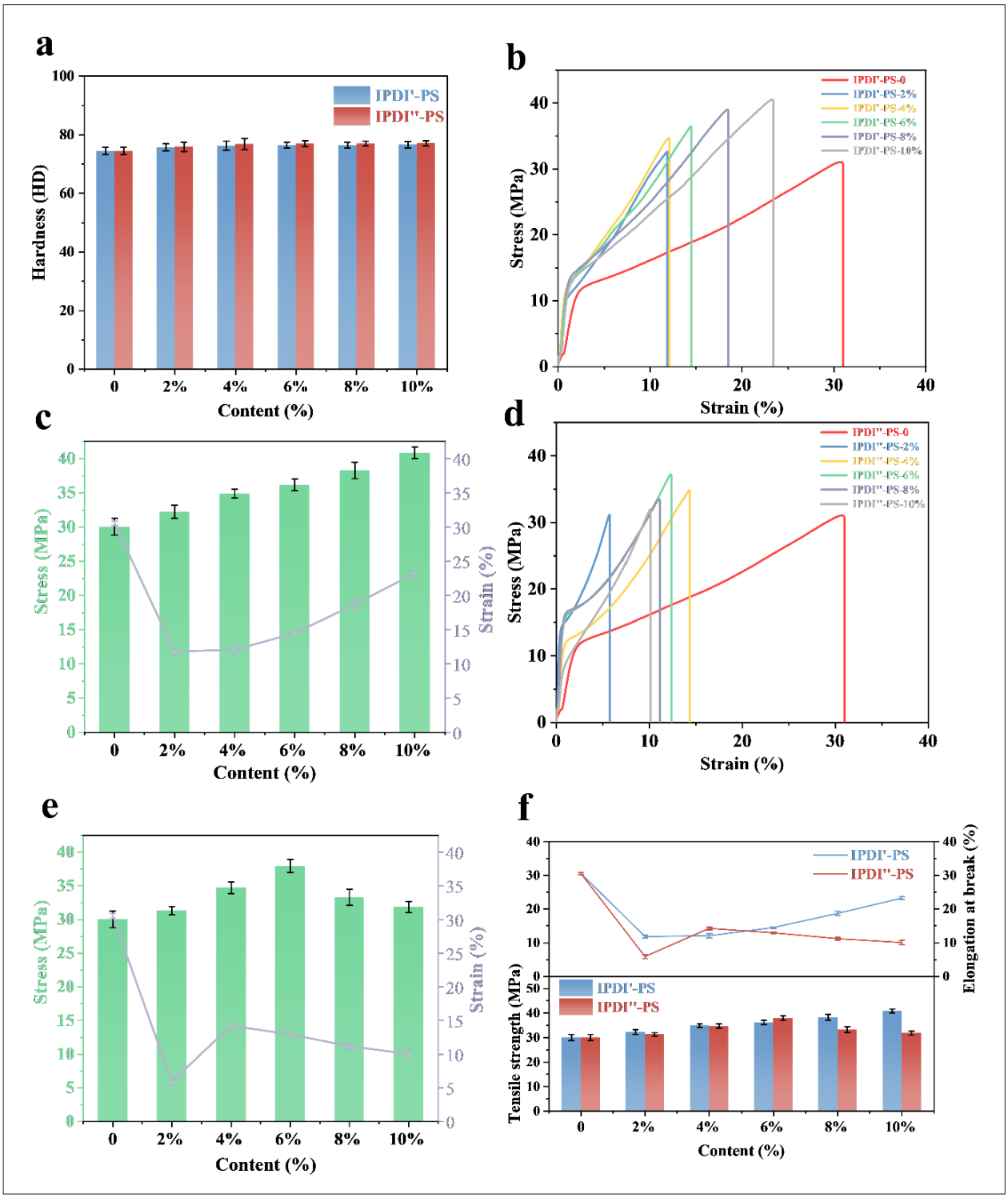


**Figure 4**. Effect of photosensitive additive content on the material's mechanical properties. (a) Hardness values of 3D-printed materials containing different loadings of IPDI'-PS or IPDI"-PS ($n$ = 5). (b) Stress–strain curves of 3D-printed materials with different IPDI'-PS loadings. (c) Tensile strength and elongation at break of 3D-printed materials modified with IPDI'-PS at different loadings ($n$ = 5). (d) Stress–strain curves of IPDI"-PS-modified 3D-printed materials at varying additive concentrations. (e) Tensile strength versus elongation at break for 3D-printed materials containing IPDI"-PS at different loadings ($n$ = 5). (f) Comparative tensile strength and elongation at break of 3D-printed resin systems incorporating IPDI'-PS or IPDI"-PS at different loadings ($n$ = 5). Abbreviations: IPDI'-PS, 3D printed photosensitive resins of monopyridine salt photosensitive additive; IPDI"-PS, 3D printed photosensitive resins of bipyridine salt photosensitive additive.

efficacy of photosensitizing additives containing pyridinium functional monomers against *S. aureus* and *E. coli* using the colony counting method. The study aimed to assess the enhancement effect on their antibacterial properties of 3D printing materials. The proposed antibacterial mechanism of pyridinium-containing groups is presented in Figure 5a. The results demonstrated that incorporating IPDI'-PS significantly enhanced the antibacterial activity of the resin (Figure 5b). Remarkably, 3D-printed samples containing only 2 wt% IPDI'-PS exhibited pronounced antibacterial effects against both common pathogens. Furthermore, antibacterial efficacy was continuously enhanced with increasing IPDI'-PS loading. Against *S. aureus*, a bactericidal rate of 99% was achieved at a 10 wt% loading. This effect was even more pronounced against *E. coli*, where a bactericidal rate as

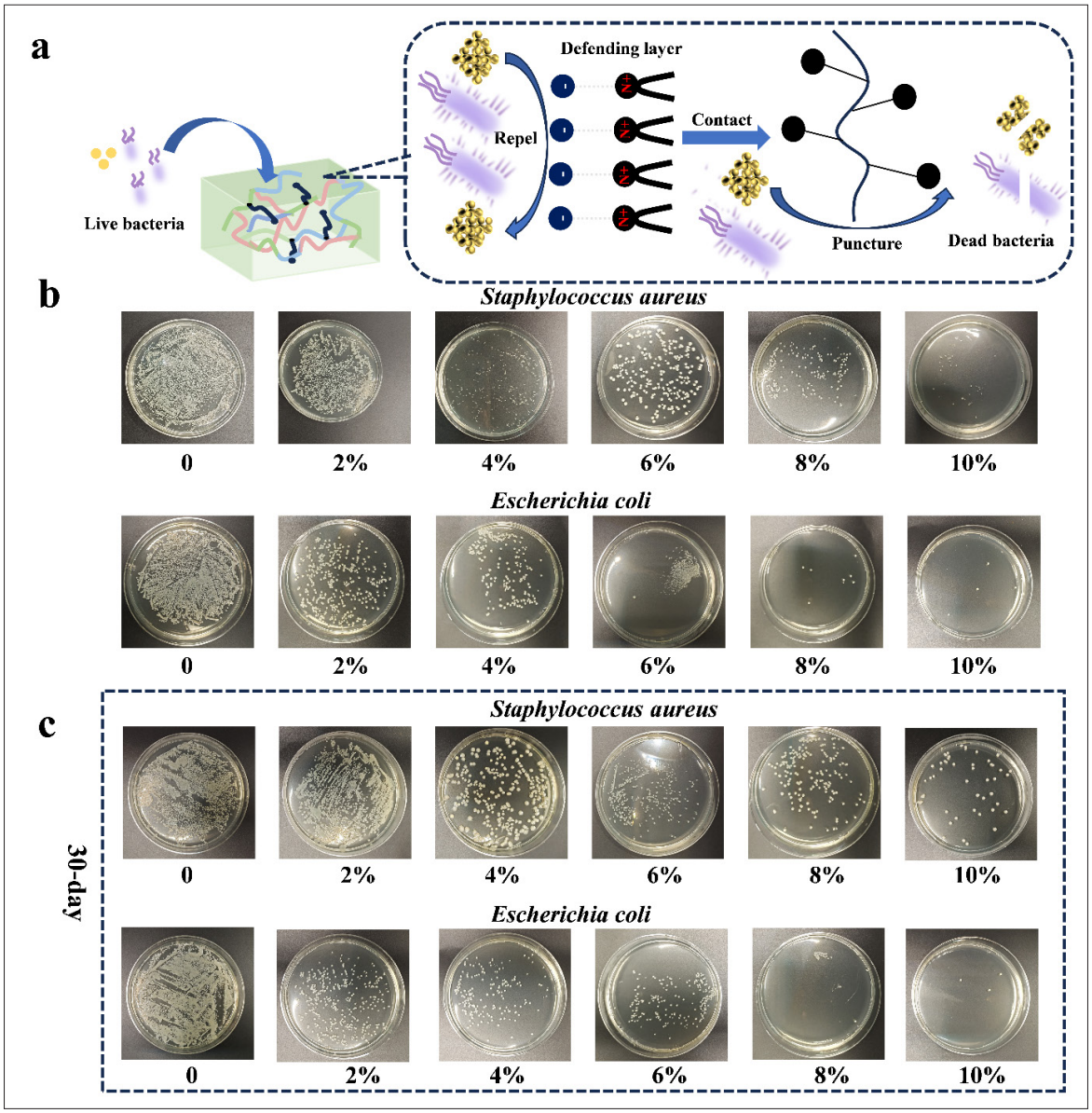


**Figure 5.** Antibacterial mechanism and evaluation of 3D printed materials. (a) Schematic of the contact-killing antibacterial mechanism of pyridinium-containing photosensitive resin. (b) Antibacterial efficacy of IPDI'-PS-modified 3D-printed materials against *Staphylococcus aureus* and *Escherichia coli* with different additive (IPDI'-PS) loadings. (c) Sustained antibacterial performance against *S. aureus* and *E. coli* after 30-day light-proof storage of IPDI'-PS-modified 3D-printed materials at various concentrations. Abbreviations: IPDI'-PS, 3D printed photosensitive resins of monopyridine salt photosensitive additive.

high as 99.99% was attained with only 8 wt% loading. To assess the durability of the antibacterial performance, the samples were stored under light-proof sealed conditions for 30 days and re-tested (Figure 5c). The results revealed no significant changes in the bactericidal rate in any group. Crucially, samples containing 10 wt% IPDI'-PS maintained a 99% bactericidal rate against *S. aureus*, whereas those with 8 wt% IPDI'-PS retained a high bactericidal rate of 99.99% against *E. coli*, presenting a negligible deviation from the initial values (Figure 6c and d). This confirms the excellent stability and long-term persistence of the synthesized pyridinium-containing molecules within the material matrix, indicating a low susceptibility to deactivation.

Similarly, the photosensitive resin composition containing dual-pyridinium IPDI"-PS demonstrated excellent antibacterial properties against *S. aureus* and *E. coli* (Figure 6a). At an ultralow IPDI"-PS loading of 2 wt%, the composition exhibited significant antibacterial activity, achieving bactericidal rates of 91% against *S. aureus* and 92% against *E. coli*. The antibacterial efficacy further increased continuously with higher IPDI"-PS loadings and plateaued at higher concentrations. For *S. aureus*, a bactericidal rate of 99% was attained at 10 wt% loading, with a diminished enhancement beyond approximately 6 wt%. Against *E. coli*, a bactericidal rate as high as 99.99% was achieved at 10 wt% loading. To evaluate durability, the samples were retested after 30 days of light-proof sealed storage (Figure 6b). The results confirmed that the IPDI"-PS system maintained high antibacterial efficacy; at 2 wt% loading, substantial activity against *S. aureus* persisted, whereas at 10 wt% loading, the bactericidal rates remained consistently high at 99% for *S. aureus* and 99.99% for *E. coli* (Figure 6e and f). Comparative analysis revealed that the IPDI"-PS system significantly outperformed the IPDI'-PS system against both the tested bacteria at equivalent loadings, particularly in the low-loading regime, with a more pronounced antibacterial advantage against *E. coli*. This validates the superiority of pyridinium-containing photosensitizing additives for enhancing the antibacterial performance of 3D printing materials.

### 3.6. Antistatic properties

Photosensitive resin-based 3D printing materials are susceptible to static charge accumulation during use, leading to printing defects, reduced material lifespan, and safety hazards.[36–38] Therefore, it is crucial to impart efficient and long-lasting antistatic properties to these materials. Pyridinium-based ionic antistatic agents have been extensively researched for their effectiveness, with their performance closely tied to molecular structural features.[39–41] The material's ability to conduct or dissipate charge is directly characterized by surface resistivity (Figure 7a).[42,43] Low resistivity (typically $\leq 10^{11}$ Ω) facilitates rapid charge migration, preventing electrostatic accumulation and providing antistatic properties. In contrast, high resistivity ($\geq 10^{12}$ Ω) encourages charge buildup, increasing electrostatic risks.[44] Therefore, this study systematically assessed the influence of photosensitive compositions containing pyridinium functional monomers with varying group counts on the antistatic performance of 3D-printed materials through surface resistivity measurements. As displayed in Figure 7b and c, the unmodified resin (devoid of pyridinium-based acrylate photosensitizing additives) demonstrated resistivity > $10^{12}$ Ω, indicating insulating behavior. The addition of any pyridinium-containing photosensitizing additive notably decreased the resistivity, with the reduction magnitude escalating with loading. Moreover, after both systems underwent light-proof storage for 14 and 60 days, followed by resistivity re-measurement, only gradual increases in resistivity were observed. Both systems exhibited consistent antistatic performance over time, affirming their exceptional persistence and low susceptibility to migration or leaching of the synthesized pyridinium-containing molecules.

A significant difference was observed between the following two systems: The IPDI"-PS composition exhibited superior efficiency. The IPDI'-PS system needed an 8 wt% loading to reduce resistivity to $10^{10}$ Ω (indicating effective antistatic performance), while the IPDI"-PS system achieved resistivity as low as $10^{9}$ Ω with just a 4 wt% loading—well within the effective electrostatic dissipation range ($10^{6}$–$10^{9}$ Ω). This performance advantage is attributed to the two PS cationic ($N^{+}$) groups in the IPDI"-PS structure, which result in a higher charge carrier concentration, thus more effectively facilitating charge migration and dissipation.

## 4. Conclusion

In this study, we synthesized acrylate photosensitive additives containing either monopyridinium salt groups (IPDI'-PS) or bispyridinium salt groups (IPDI"-PS) using IPDI as the starting material. The synthesis involved chain extension through a reaction with a polyol, followed by HEMA functionalization and subsequent quaternization with 4-AP. These additives were then integrated into a photosensitive resin matrix at 0–10 wt%. The specimens were fabricated using DLP 3D printing. The study aimed to investigate the effects of the number of pyridinium salt groups and additive loading on the thermal and mechanical properties, curing shrinkage, antibacterial activity, and antistatic performance of 3D-printed materials.

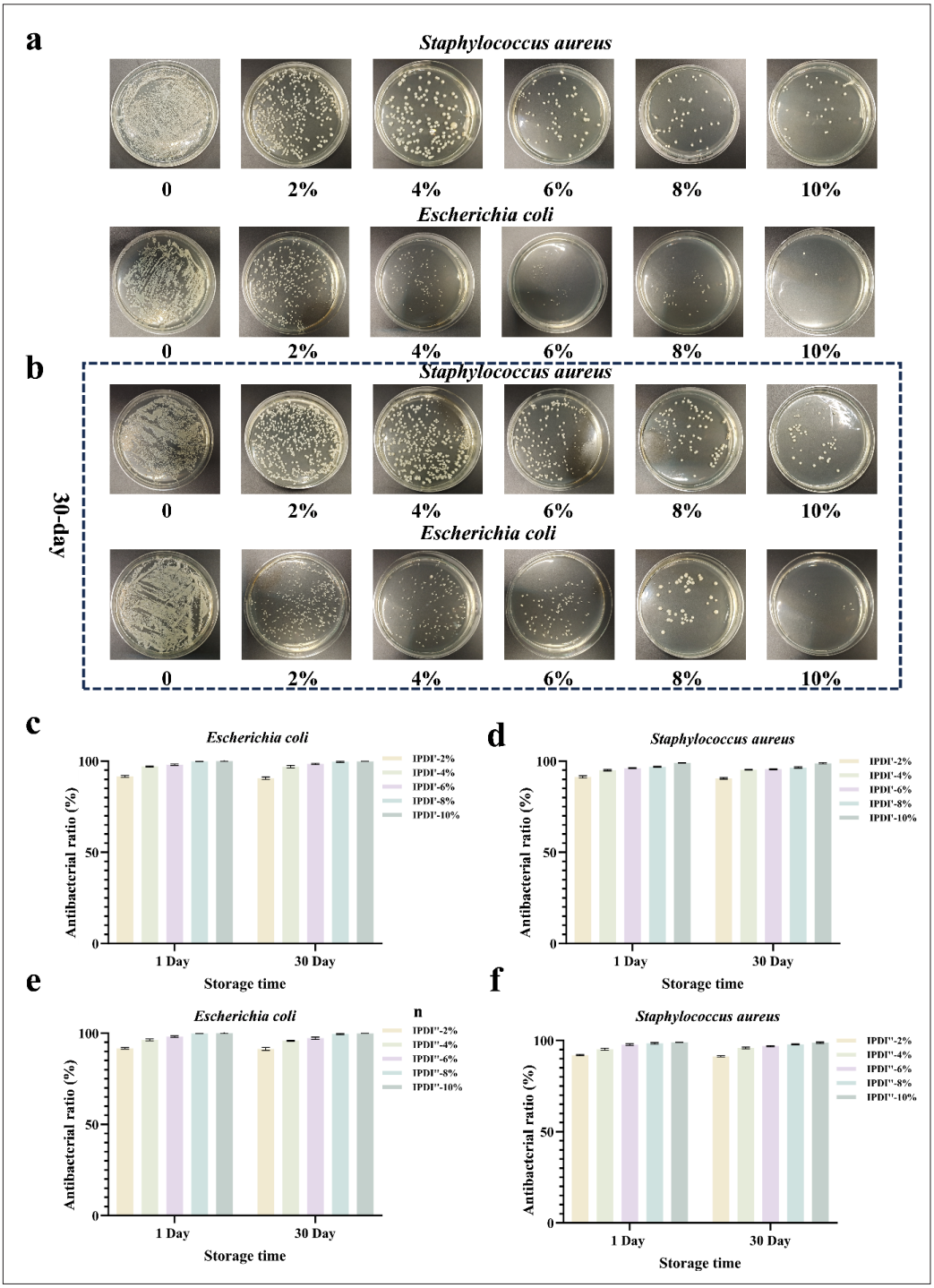


**Figure 6**. Antibacterial performance testing for 3D printed materials. (a) Antibacterial efficacy of IPDI"-PS-modified 3D-printed materials against *Staphylococcus aureus* and *Escherichia coli* at different additive (IPDI"-PS) loadings. (b) Retained antibacterial performance against *S. aureus* and *E. coli* after 30 days of light-proof storage at varying concentrations of IPDI"-PS-modified 3D-printed materials. (c) Time-dependent antibacterial efficiency against *E. coli* during extended storage of IPDI'-PS-modified 3D-printed materials at different additive (IPDI'-PS) loadings ($n$ = 5). (d) Antibacterial efficiency against *S. aureus* as a function of storage duration for IPDI'-PS-modified 3D-printed materials at varying additive (IPDI'-PS) concentrations ($n$ = 5). (e) Changes in antibacterial activity against *E. coli* over storage time for IPDI"-PS-modified 3D-printed materials at different loadings ($n$ = 5). (f) Storage-time dependence of antibacterial efficacy against *S. aureus* for IPDI"-PS 3D-printed materials at various concentrations ($n$ = 5). Abbreviations: IPDI'-PS, 3D printed photosensitive resins with different contents of monopyridine salt photosensitive additives; IPDI"-PS, 3D printed photosensitive resins with different contents of bipyridine salt photosensitive additives.

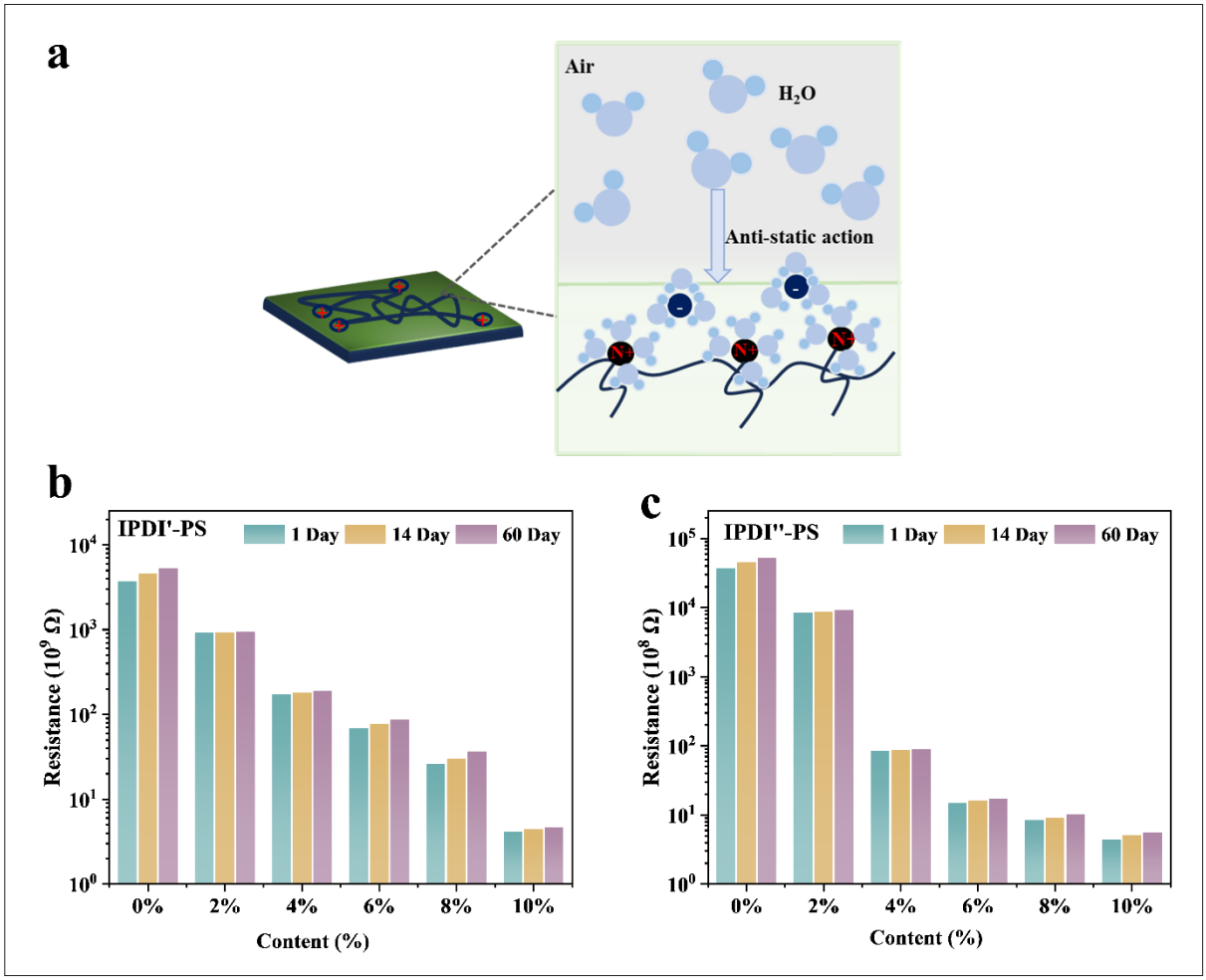


**Figure 7.** Antistatic mechanism and performance testing of 3D printed materials. (a) Antistatic mechanism of photosensitive resin containing pyridinium salt groups. (b) Resistivity changes in 3D-printed materials with IPDI'-PS at various concentration levels after different storage periods. (c) Resistivity changes in 3D-printed materials with IPDI"-PS at different concentration levels after various storage durations. Abbreviations: IPDI'-PS, 3D printed photosensitive resins of monopyridine salt photosensitive additive; IPDI"-PS, 3D printed photosensitive resins of bipyridine salt photosensitive additive.

The experimental results indicated that the cured materials containing IPDI'-PS within the photosensitive resin demonstrated superior mechanical strength and thermal stability. In contrast, the materials incorporating IPDI"-PS exhibited high antibacterial efficacy, excellent antistatic performance, and low curing shrinkage.

In the IPDI'-PS system, the best combination for overall performance was attained at a 10 wt% additive loading, resulting in a tensile strength of 40.86 MPa (a 36.0% increase compared to the control), a 30.6% increase in elongation at break, and a $T_D5$ of 168°C.

In the IPDI"-PS system, the ideal composition for overall performance was 4 wt% additive loading, leading to an HDT of 44.6 °C. The volume resistivity decreased to $10^9$ Ω, entering the effective antistatic range, with a curing shrinkage as low as 6.05%. Additionally, it exhibited a 99.99% bactericidal rate against *E. coli*.

Compared to the unmodified resin, the IPDI"-PS system, with bis-pyridinium salt groups, exhibited significantly enhanced functional efficiency. It achieved over 91% antibacterial efficacy at a low loading (2 wt%), while the IPDI'-PS system needed 8 wt% for similar efficacy. Furthermore, the IPDI"-PS system required only half the additive loading (50% reduction) for equivalent antistatic performance. The inclusion of pyridinium salt-based acrylate photosensitive additives provided long-term stability to these materials. After 30 days of dark storage, the antibacterial rate remained above 99%, and the resistivity stayed within the original order of magnitude. These enduring antistatic and antibacterial

properties highlight the material's potential, enabling the development of efficient 3D printing resins with a single low-loading additive, offering high mechanical strength and durable antibacterial/antistatic functionality. However, while pyridinium salt-based acrylate photosensitive additives effectively enhance the strength and functionality (e.g., antibacterial/antistatic properties) of 3D-printed photopolymer resins, their low solubility in the resin system raises viscosity, affecting printing reliability and resolution. Furthermore, their poor biocompatibility limits their use in non-implantable scenarios.

## Acknowledgments

The authors are grateful to the Key Laboratory of Organosilicon Chemistry and Materials Technology, Ministry of Education, for providing analytical instrument support and Eceshi (www.eceshi.com) for conducting the tests related to liquid photosensitive resin.

## Funding

This work was financially supported by Hangzhou Normal University (grant nos. 114095F49123259 and 4095F49123037).

## Conflict of interest

The authors declare no conflict of interest.

## Author contributions

*Conceptualization*: Xiaomin Zhang, Guoqiao Lai, Qiu Chen
*Formal analysis:* Qiaoling Zhang, Zhiwei Zhang, Taojun Lin
*Investigation:* Qiaoling Zhang, Tongyi Wu, Xiangqin Ding, Rong Li
*Methodology*: Qiaoling Zhang, Tongyi Wu, Jianqing Liang, Taojun Lin
*Visualization:* Qiaoling Zhang, Tongyi Wu, Taojun Lin, Xiangqin Ding
*Writing–original draft:* Qiaoling Zhang, Tongyi Wu, Xiangqin Ding
*Writing–review & editing:* Xiaomin Zhang, Guoqiao Lai, Qiu Chen

## Ethics approval and consent to participate

Not applicable.

## Consent for publication

Not applicable.

## Availability of data

Experimental data and details of the materials used in the study can be obtained from the corresponding authors upon request.

## References

1. Stevens LM, Almada NT, Kim HS, Page ZA. Visible-light-fueled polymerizations for 3D printing. *Accounts Chem Res*. 2025;58(2):250-260.
doi: 10.1021/acs.accounts.4c00680

2. Wu T, Ding X, Yuan K, Liu T, Lai G, Chen Q. Synthesis and characterization of silicon-modified polyurethane acrylate for UV-thermal dual curing in three dimensional printing. *ACS Appl Polym Mater*. 2024;6(14):8585-8597.
doi: 10.1021/acsapm.4c01581

3. Quan H, Zhang T, Xu H, Luo S, Nie J, Zhu X. Photo-curing 3D printing technique and its challenges. *Bioact Mater*. 2020;5(1):110-115.
doi: 10.1016/j.bioactmat.2019.12.003

4. Gao W, Guo Y, Cui J, *et al*. Dual-curing polymer systems for photo-curing 3D printing. *Addit Manuf*. 2024;85:104142.
doi: 10.1016/j.addma.2024.104142

5. Zheng M-Y, Jin Z-B, Ma Z-Z, Gu Z-G, Zhang J. Photo-curable 3D printing of circularly polarized afterglow metal–organic framework monoliths. *Adv Mater*. 2024;36(25):2313749.
doi: 10.1002/adma.202313749

6. He C-F, Sun Y, Liu N, Yu K, Qian Y, He Y. Formation theory and printability of photocurable hydrogel for 3D bioprinting. *Adv Funct Mater*. 2023;33(29):2301209.
doi: 10.1002/adfm.202301209

7. Wu T, Zhang Q, Zhang Z, *et al*. Multiple hydrogen bonded 3D-printed elastomers with enhanced toughening by photothermal dual curing for customizable biomimetic flexible grippers. *Adv Funct Mater*. 2025;e10489.
doi: 10.1002/adfm.202510489

8. Mu X, Bertron T, Dunn C, *et al*. Porous polymeric materials by 3D printing of photocurable resin. *Mater Horiz*. 2017;4(3):442-449.
doi: 10.1039/C7MH00084G

9. Sun X, Chen S, Qu B, *et al*. Light-oriented 3D printing of liquid crystal/photocurable resins and in-situ enhancement of mechanical performance. *Nat Commun*. 2023; 14(1):6586.
doi: 10.1038/s41467-023-42369-1

10. You J-L, Liu IT, Chen Y-H, Balaji R, Tung S-H, Liao Y-C. Adamantane-based low-dielectric-constant photocurable resin for 3D printing electronics. *Addit Manuf*. 2024;82:104047.

doi: 10.1016/j.addma.2024.104047

11. Zhang T, Chen D, Zhang N, *et al*. Self-assembled supramolecular nanofibers integrate pH-responsive drug delivery and antimicrobial for combined cancer therapy. *Chinese Chem Lett*. 2025;111117. doi: 10.1016/j.cclet.2025.111117
12. Zhong G, Deng S, Hong Y, *et al*. AIE-active antibacterial photosensitizer disrupting bacterial structure: multicenter validation against drug-resistant pathogens. *Small Methods*. 2025;9(5):2401663. doi: 10.1002/smtd.202401663
13. Zhu Y, Qin L, Yang M, *et al*. Dual-functional benzotrithiophene-based covalent organic frameworks for photocatalytic detoxification of mustard gas simulants and antibacterial defense. *Small*. 2025;21(12):2412118. doi: 10.1002/smll.202412118
14. Tang X, Yan G, Wang J, *et al*. Self-assembly and antistatic property of ionic liquid crystalline polymers. *Polym Adv Technol*. 2022;33(5):1628-1641. doi: 10.1002/pat.5626
15. Zhuang Y, Tang X, Chang X, *et al*. Self-assembly and antistatic property of poly(styrene sulfonic acid)-based graphene oxide liquid crystal compounds. *Liquid Crystals*. 2022;49(5):731-741. doi: 10.1080/02678292.2021.2006810
16. Ma Q, Buchon L, Magné V, *et al*. Charge transfer complexes (CTCs) with pyridinium salts: toward efficient dual photochemical/thermal initiators and 3D printing applications. *Macromol Rapid Commun*. 2022;43(19):2200314. doi: 10.1002/marc.202200314
17. Goldbach E, Allonas X, Halbardier L, Ley C, Croutxé-Barghorn C. Use of pyridine derivatives as inhibitor/retarding agent for photoinduced cationic polymerization of epoxides. *React Funct Polym*. 2024;200:105922. doi: 10.1016/j.reactfunctpolym.2024.105922
18. Zhou Q, Chen S, Guo X, Zhou C, Jin M. New water-soluble coumarin-ketone-pyridium salts photoinitiators for antibacterial coatings under visible LED photocuring. *Eur Polym J*. 2025;230:113896. doi: 10.1016/j.eurpolymj.2025.113896
19. Wu T, Zhang Q, Xie Z, *et al*. High dispersibility Organosilicon@ZnO-NPs prepared by spray sedimentation method: similar chain extender enhances the strength, antimicrobial, and UV shielding of 3D printing composite materials. *Compos Part B Eng*. 2025;295:112196. doi: 10.1016/j.compositesb.2025.112196
20. Jarach N, Cohen M, Gitt R, Dodiuk H, Kenig S, Magdassi S. Untying the knot: a fully recyclable, solvent-free, wide-spectral photocurable thermoset adhesive. *Adv Mater*. 2025;37:e2502040. doi: 10.1002/adma.202502040
21. Lv Y, Xu Y, Zhang S, *et al*. Rapidly photocurable and strongly adhesive hydrogel-based sealant with good procoagulant activity for lethal hemorrhage control. *Adv Funct Mater*. 2025;e2501904. doi: 10.1002/adfm.202501904
22. Hu P, Xu H, Pan Y, Sang X, Liu R. Upconversion particle-assisted NIR polymerization enables microdomain gradient photopolymerization at inter-particulate length scale. *Nat Commun*. 2023;14(1):3653. doi: 10.1038/s41467-023-39440-2
23. Chen Q, Liu Y, Peng X, *et al*. A novel photosensitive poly(amic acid) for reducing film thickness shrinkage after curing. *Mater Today Commun*. 2025;47:113210. doi: 10.1016/j.mtcomm.2025.113210
24. Ding A, Zhang P, Zhou B, *et al*. Structural design and performance study of a biobased UV/moisture dual-curing coating for UV inadequate curing conditions. *Mater Today Commun*. 2025;44:111863. doi: 10.1016/j.mtcomm.2025.111863
25. Sun G, Wu X, Liu R. A comprehensive investigation of acrylates photopolymerization shrinkage stress from micro and macro perspectives by real time MIR-photo-rheology. *Prog Org Coat*. 2021;155:106229. doi: 10.1016/j.porgcoat.2021.106229
26. Wang J, Li J, Wang X, *et al*. Synthesis and properties of UV-curable polyester acrylate resins from biodegradable poly(l-lactide) and poly(ε-caprolactone). *React Funct Polym*. 2020;155:104695. doi: 10.1016/j.reactfunctpolym.2020.104695
27. Xiao N, Zhang Y, Gao Y, Hu D, Sun F. A dual-functional α-diketone-based disulfide monomer for visible LED photopolymerization: mitigating volumetric shrinkage and triggering polymerization. *Eur Polym J*. 2024;217:113341. doi: 10.1016/j.eurpolymj.2024.113341
28. Zhu G, Liu M, Kou Z, *et al*. Universal approach for developing reprocessable and reprintable plant oil-based resins for digital light processing 3D printing. *Chem Eng J*. 2023;475:146080. doi: 10.1016/j.cej.2023.146080
29. Alhajj M, Liau LS, Al-Fakih AM. Polymer electrolytes for sustainable energy: a minireview on zero-carbon storage and conversion. *ACS Appl Polym Mater*. 2025;7(6):3442-3465. doi: 10.1021/acsapm.4c03958
30. Wang W, Li X, Gao L, *et al*. Thermal cross-linking hole-transport self-assembled monolayers for perovskite solar cells. *ACS Energy Lett*. 2025;10(5):2250-2258.

doi: 10.1021/acsenergylett.5c00457

31. Jamal M, Benkaddour A, Pal L, *et al*. Multi-scale assembly and structure-process-property relationships in nanocellulosic materials. *Prog Mater Sci*. 2025;151:101430. doi: 10.1016/j.pmatsci.2025.101430

32. Richbourg NR, Peppas NA. The swollen polymer network hypothesis: quantitative models of hydrogel swelling, stiffness, and solute transport. *Prog Polym Sci*. 2020;105:101243. doi: 10.1016/j.progpolymsci.2020.101243

33. Huang Y-W, Torkelson JM. Catalyst-free polyhydroxyurethane covalent adaptable networks exhibiting full cross-link density recovery after reprocessing: facilitation by synthesis with well-designed secondary amines. *Macromolecules*. 2025;58(10):5356-5367. doi: 10.1021/acs.macromol.5c00280

34. Mao H-I, Chen Y-Z, Chu R-J, *et al*. Recyclable thermoset-like polyurethanes from renewable epoxidized soybean oil via dynamic ester bond exchange. *J Polym Sci*. 2025;63(11):2379-2390. doi: 10.1002/pol.20250378

35. Zhang Z, Liu G, Wu J, *et al*. High-strength dual-network hydrogels with chain-growth enhancement for multifunctional flexible sensors, triboelectric nanogenerators, and EMI shielding. *Chem Eng J*. 2025;519:165710. doi: 10.1016/j.cej.2025.165710

36. Sun Q, Xu B, Du J, *et al*. Interfacial electrostatic charges promoted chemistry: reactions and mechanisms. *Adv Colloid Interface Sci*. 2025;339:103436. doi: 10.1016/j.cis.2025.103436

37. Koochak P, Lin M, Afzalifar A, *et al*. Self-accelerating drops on silicone-based super liquid-repellent surfaces. *ACS Nano*. 2025;19(25):23105-23119. doi: 10.1021/acsnano.5c04250

38. Nie J, Sun B, Jiao T, *et al*. Biodegradable air filter with electrospun composite nanofibers and cellulose fibers dual network: enhanced electrostatic adsorption, humidity resistance, and extended service life. *J Hazard Mater*. 2025;489:137557. doi: 10.1016/j.jhazmat.2025.137557

39. Sun N, Yi C, Xu C, *et al*. Fabrication of permanent antistatic PMMA copolymer for enhanced antistatic and mechanical properties. *ACS Appl Polym Mater*. 2023;5(7):5537-5543. doi: 10.1021/acsapm.3c00833

40. Ren J, Zheng L, Wang Y, *et al*. Synthesis and characterization of quaternary ammonium based ionic liquids and its antistatic applications for diesel. *Colloids Surf A Physicochem Eng Asp*. 2018;556:239-247. doi: 10.1016/j.colsurfa.2018.08.038

41. Tsurumaki A, Iwata T, Tokuda M, *et al*. Polymerized ionic liquids as durable antistatic agents for polyether-based polyurethanes. *Electrochim Acta*. 2019;308:115-120. doi: 10.1016/j.electacta.2019.04.031

42. Bera M, De B, Gupta KBNVSG, *et al*. A critical review on recent progress in anti-static fiber-reinforced polymer (FRP) composites. *Polym Compos*. 2025;e70078. doi: 10.1002/pc.70078

43. Yousefi E, Dolati A, Najafkhani H. Preparation of robust antistatic waterborne polyurethane coating. *Prog Org Coat*. 2020;139:105450. doi: 10.1016/j.porgcoat.2019.105450

44. Huang Z, Yin L, Hu C, *et al*. Low contact resistivity and long-term thermal stability of Nb0.8Ti0.2FeSb/Ti thermoelectric junction. *J Mater Sci Technol*. 2020;40:113-118. doi: 10.1016/j.jmst.2019.08.046